

Dense nitrogen-enriched circumnuclear region of the new high-redshift quasar ULAS J0816+2134 at $z = 7.46$

EKATERINA KOPTILOVA¹ AND CHORNG-YUAN HWANG¹

¹*Graduate Institute of Astronomy
National Central University
Taoyuan City 32001, Taiwan*

(Received December 12, 2022)

Submitted to ApJ

ABSTRACT

We present the $0.85 - 2.5 \mu\text{m}$ discovery spectrum and multi-epoch photometry of the new high-redshift quasar ULAS J081621.47+213442.6 obtained using the GNIRS spectrograph of the Gemini North and near-infrared wide-field camera of the 4-m UKIRT telescopes. The redshift of ULAS J081621.47+213442.6 measured from the Mg II $\lambda 2799$ emission line is $z_{\text{MgII}} = 7.461 \pm 0.007$. The absolute magnitude of the quasar is $M_{1450} = -25.33 \pm 0.07$. The black hole mass estimated using the Mg II $\lambda 2799$ line and Eddington accretion rate are $M_{\text{BH}} \sim 5 \times 10^8 M_{\odot}$ and $L_{\text{bol}}/L_{\text{Edd}} \sim 0.7$. The spectrum of ULAS J081621.47+213442.6 exhibits strong N III] $\lambda 1750$ emission line of a rest-frame equivalent width of $\text{EW}_0 \gtrsim 12.5 \text{\AA}$. The high abundance of nitrogen suggests that ULAS J081621.47+213442.6 may be at the peak of the nitrogen enrichment of the circumnuclear region by the asymptotic giant branch stars, which is expected $\sim 0.25 \text{ Gyr}$ after the bulk of star formation. The age of the starburst of ULAS J081621.47+213442.6 implied by the high nitrogen abundance, indicates that the active phase of the black hole growth of the quasar may have lasted only $\sim 0.25 \text{ Gyr}$, favoring a massive initial black hole seed. We also observed the flux variations of the UV continuum of ULAS J081621.47+213442.6 caused by the variation in the line-of-sight absorbing column density on a rest-frame timescale of $\sim 47 \text{ d}$. The estimated hydrogen column density of the gas cloud responsible for this variation is $N_{\text{H}} \gtrsim 10^{23.5} \text{ cm}^{-2}$, consistent with the typical column density of mostly neutral, gravitationally bound clouds of the broad line region of quasars.

Keywords: quasars: emission lines — quasars: supermassive black holes — quasars: individual (ULAS J081621.47+213442.6)

1. INTRODUCTION

High-redshift quasars at $z \lesssim 7$ discovered in different sky surveys (e.g., Willott et al. 2010a; Mortlock et al. 2011; Venemans et al. 2013, 2015; Jiang et al. 2016; Bañados et al. 2016; Wang et al. 2018; Matsuoka et al. 2019; Wang et al. 2019; Yang et al. 2019; Reed et al. 2019; Matsuoka et al. 2022) already harbor supermassive black holes (SMBHs) of typical masses $10^8 - 10^9 M_{\odot}$ at a cosmic age of $\lesssim 1 \text{ Gyr}$. The SMBHs of these quasars are still in the phase of intensive growth as implied by their near-Eddington accretion rates (e.g., Willott et al.

2010b; De Rosa et al. 2011; Mazzucchelli et al. 2017). On the other hand, the discovery of the BL Lac object at $z \approx 6.6$ suggests that the SMBHs of some of the high-redshift quasars may have already finished the growth by the end of the reionization epoch (Koptelova & Hwang 2022).

The massive SMBHs of $\sim 10^9 M_{\odot}$ were also found at the centers of the most distant of the known high-redshift quasars, J1342+0928 at $z_{[\text{CII}]} = 7.541$ ($M_{1450} = -26.76$; Bañados et al. 2018), J1007+2115 at $z_{[\text{CII}]} = 7.515$ ($M_{1450} = -26.66$ Yang et al. 2020), and J0313-1806 at $z_{[\text{CII}]} = 7.642$ ($M_{1450} = -26.13$ Wang et al. 2021). The cosmic age of $\lesssim 0.7 \text{ Gyr}$ corresponding to the redshifts of these quasars provides strong constraints on the formation timescale of the first SMBHs. However,

the details of their formation process remain elusive (for a review, see [Inayoshi et al. 2020](#)). Assuming the Eddington limited growth rate from $z \sim 30$, the $\sim 10^9 M_\odot$ SMBH masses of these quasars should have grown from initial seeds of $10^3 - 10^5 M_\odot$ (e.g., [Wang et al. 2021](#)).

The measurements of the metal abundance in high-redshift quasars from different broad (e.g., [Hamann et al. 2002](#); [Dietrich et al. 2003a,b](#); [Nagao et al. 2006a](#); [Jiang et al. 2007](#); [Juarez et al. 2009](#); [De Rosa et al. 2014](#)) and narrow (e.g., [Nagao et al. 2006b](#); [Matsuoka et al. 2009](#)) emission lines are consistent with the supersolar metallicity of their circumnuclear gas even at $z \sim 7.5$ (e.g., [Onoue et al. 2020](#)) and imply the early chemical enrichment (e.g., [Hamann & Ferland 1992, 1993](#)). For example, from the eight line ratios with different nitrogen lines of 70 high-redshift quasars at $3.5 < z < 5.0$, [Dietrich et al. \(2003b\)](#) inferred a mean metallicity of the broad line region gas of $5.3 \pm 0.3 Z_\odot$ (see also [Dietrich et al. 2003a](#)). Similar metallicities were also derived for smaller samples, e.g., from the N V/C IV and N V/He II line ratios of 6 quasars at $5.8 < z < 6.3$, [Jiang et al. \(2007\)](#) inferred a mean metallicity of $\sim 4 Z_\odot$, whereas [Juarez et al. \(2009\)](#) inferred a metallicity of $\sim 7 Z_\odot$ from analysis of the (Si IV $\lambda 1397 +$ O IV $\lambda 1402$)/C IV $\lambda 1549$ ratios of 30 quasars at $4.0 < z < 6.4$.

The method for constraining the epoch of first star formation in the host galaxies of high-redshift quasars usually employs the Fe II/Mg II line ratio and is based on the delay in the Fe enrichment relative to Mg by approximately 1 Gyr ([Hamann & Ferland 1993](#)). No evolution of this line ratio with redshift was convincingly measured up to $z \sim 7.5$ (e.g., [Maiolino et al. 2003](#); [De Rosa et al. 2011](#); [Mazzucchelli et al. 2017](#); [Onoue et al. 2020](#); [Schindler et al. 2020](#)).

Alternatively, the age of the starburst can be constrained based on the abundance of nitrogen relative to C and O ([Edmunds & Pagel 1978](#); [Hamann & Ferland 1992](#)). Nitrogen is mainly synthesized as a secondary element from the previously produced C and O, which results in the delayed nitrogen enrichment with a characteristic time lag of ~ 0.25 Gyr ([Charlot & Bruzual 1991](#); [Henry et al. 2000](#); [Johnson et al. 2022](#)). The dominant source of nitrogen are stars in the asymptotic giant branch (AGB) phase in a mass range of $4 M_\odot \lesssim m \lesssim 8 M_\odot$ (with lifetimes $\sim 2 \times 10^8$ and $\sim 4 \times 10^7$ yr, respectively) ([Hamann & Ferland 1993](#); [Charlot & Bruzual 1991](#); [Henry et al. 2000](#)). These stars have higher metallicities compared to the preceding generation of short-lived ($< 4 \times 10^7$ yr) massive stars and therefore can produce larger amounts of N.

At the bulk of star formation, the chemical enrichment is driven by massive stars with the largest C/N and the lowest N/O ratios. The cosmological hydrodynamical simulations of chemical enrichment predict the sharp local minimum in the C/N ratio at the onset of the AGB stars when these stars start to release N ([Vincenzo & Kobayashi 2018a,b](#)). The chemical evolution model of [Valiante et al. \(2009\)](#) predicts that the AGB stars may dominate the dust production on timescales of $\gtrsim 0.15$ Gyr. After the onset of the AGB stars, the C/N ratio is expected to increase due to the delayed release of C by less massive AGB stars, and then decrease again on long timescales due to the opposite dependence of the C and N stellar yields on metallicity. Thus, the detection of the increased nitrogen abundance expected ~ 0.25 Gyr after the bulk of star formation can provide the approximate age of the starburst.

The observations show that the Eddington ratios of quasars correlate with the abundance of nitrogen in their broad line regions ([Matsuoka et al. 2011, 2017](#)). Thus, from the analysis of the optical spectra of the 2383 SDSS quasars at $2.3 \lesssim z \lesssim 3.0$, [Matsuoka et al. \(2011\)](#) found that the quasars with the higher N V/C IV and N V/He II line ratios have higher Eddington ratios. The black holes of some of the known high-redshift quasars at $z \sim 6.1 - 6.6$ showing high N V/C IV line ratios are indeed among the most actively growing SMBHs at early epochs accreting at the super-Eddington accretion rates (e.g., [Kurk et al. 2009](#); [Koptelova et al. 2019](#)). [Matsuoka et al. \(2017\)](#) also found that the Eddington ratios and masses of the SMBHs of the nitrogen-rich quasars are correspondingly high and low in comparison with normal quasars and that the strong nitrogen lines of these quasars result not from their high metallicities but from the high abundance of nitrogen in their circumnuclear regions ([Araki et al. 2012](#); [Matsuoka et al. 2017](#)). A similar conclusion about the high nitrogen abundance of nitrogen-rich quasars was obtained by [Batra & Baldwin \(2014\)](#), although they interpreted the high abundance of nitrogen as due to the generally higher metallicities of nitrogen-rich quasars compared to normal quasars. It was suggested that the high accretion rates of quasars with the high relative abundance of nitrogen result from the mass loss of the AGB stars ([Padovani & Matteucci 1993](#); [Davies et al. 2007](#); [Matsuoka et al. 2011, 2017](#)). The material released by these stars enriches the host galaxies of quasars with nitrogen and also fuels the growth of their SMBHs.

The flux ratios between different broad emission lines depend not only on metallicity, but also on physical conditions in the broad line region such as the level of ionization, column density, and number density of

gas (e.g., Marziani et al. 2020). The broad line region gas is commonly represented as a system of line emitting clouds of densities $n_{\text{H}} \sim 10^9 - 10^{10} \text{ cm}^{-3}$ and linear sizes of $\sim 10^{13} - 10^{14} \text{ cm}$ orbiting at distances $\sim 10^{16} - 10^{17} \text{ cm}$ from the central black hole (for a review, see, e.g., Netzer 2008; Gaskell 2009). Observational evidence for the clumpy structure of the broad line region is provided by the variation of the X-ray flux of Seyfert galaxies caused by the motion of the absorbing/obscuring clouds through the line of sight to the ionizing continuum (Risaliti et al. 2002, 2007, 2009, 2011; Gallo et al. 2021). The observation of the partial obscuration of the X-ray continuum emitting region by these clouds provides constraints on the properties of the clouds. For instance, Risaliti et al. (2009) showed that the variation of the X-ray flux of the Seyfert galaxy NGC 1365 was caused by the change in the partial obscuration of the X-ray emitting region by a cloud of size $\sim 10^{13} \text{ cm}$, column density of $N_{\text{H}} \sim 10^{23} \text{ cm}^{-2}$, moving at a distance of $\sim 10^{16} \text{ cm}$ from the central black hole. The photoionization calculations of Wang et al. (2012) predict that similar to the X-ray emission, the UV emission of quasars can also be significantly affected by absorption/obscuration caused by the broad line region clouds. The observation of the obscuration of the UV emitting region by such clouds can provide constraints on the linear size and column density of the clouds similar to those obtained, e.g., by Risaliti et al. (2007, 2011); Gallo et al. (2021)

In this work, we present the spectroscopic confirmation of a new distant quasar, ULAS J081621.47+213442.6 at $z_{\text{MgII}} = 7.461$ (hereafter ULAS J0816+2134). The spectrum of ULAS J0816+2134 shows the strong N III $\lambda 1750$ emission line, which provides constraints on the starburst age of its host galaxy. The multi-epoch observations of the rest-frame UV continuum of ULAS J0816+2134 in the J band, revealed significant variability attributed to the variation in the line-of-sight absorbing column density. In Section 2, we describe the observational data. In Section 3, we present the analysis of the spectral properties and the J , H , and K -band light curves of ULAS J0816+2134. In Section 4, we provide the measurement of the black holes mass, discuss the growth history of the black hole, and obtain constraints on the column density and size of the gas clouds in the broad line region of ULAS J0816+2134. In the paper, we assume a flat cosmology with Hubble constant $H_0 = 70 \text{ km s}^{-1} \text{ Mpc}^{-1}$, mass density $\Omega_{\text{m}} = 0.3$, and vacuum density $\Omega_{\Lambda} = 0.7$.

2. OBSERVATIONS

2.1. Broad-band Photometry

ULAS J0816+2134 was selected using the catalogs of three different surveys: the Panoramic Survey Telescope and Rapid Response System 1 (PS1; Chambers et al. 2016), United Kingdom Infrared Telescope (UKIRT) Infrared Deep Sky Survey Large Area Survey (UKIDSS LAS; Lawrence et al. 2007), and Wide-field Infrared Survey Explorer (WISE; Wright et al. 2010; Cutri et al. 2014). The selection procedure employed the following selection criteria: the detection in the UKIDSS J , WISE $W1$, and $W2$ bands with approximate colors $J - W1 > -0.1$ and $W1 - W2 > 0$ AB mag expected for quasars at $z \gtrsim 6$, and the non-detection in all PS1 bands. ULAS J0816+2134 was observed by UKIDSS LAS at two different epochs, in 2007 in the J band and in 2008 in the Y , J , H , and K bands. In 2007, the J -band brightness of this object was below the detection limit of the survey. In 2008, ULAS J0816+2134 was detected in the J , H , and K bands, but not in the Y band (see Table 1). The non-detection in the PS1 and UKIDSS LAS Y bands, infrared color, and J -band variability of > 1 mag suggested that this object is a likely candidate for a high-redshift quasar.

The deeper UKIRT Z -, Y -, J -, H -, and K -band images of ULAS J0816+2134 were obtained on 2021 February 3, on 2022 January 27 and March 13. The near-infrared magnitudes of ULAS J0816+2134 from these observations are also presented in Table 1. These recent images were reduced using the same automated pipeline as the images of the UKIDSS LAS survey (see Hewett et al. 2006). Note that the photometric catalog released by the UKIDSS LAS survey provides only the J -band magnitude of ULAS J0816+2134 corresponding to epoch 2008 (as given in Table 1). The H and K magnitudes from the same epoch were not reported, likely due to the marginal detection of ULAS J0816+2134 in both UKIDSS LAS H - and K -band images. The UKIDSS LAS H and K magnitudes provided in Table 1 were estimated by us from the stack images obtained by this sky survey and available at the UKIRT WFCAM Science Archive (WSA)¹. The resulting magnitudes and the magnitude uncertainties quoted in the table represent the average values and the standard deviations of six different flux measurements relative to different nearby stars in each of the H - and K -band UKIDSS images. The mid-infrared magnitudes of ULAS J0816+2134 provided in Table 1 are from the AllWISE catalog of Cutri et al. (2014).

¹ <http://wsa.roe.ac.uk/>

2.2. Near-infrared Spectroscopy

The spectroscopic observations of ULAS J0816+2134 were conducted on 2021 May 1, 4, and 17 using the Gemini Multi-Object Spectrograph (Gemini-N/GNIRS; Elias et al. 2006) in the cross-dispersed mode, which provided a spectral coverage of $\sim 0.85 - 2.5 \mu\text{m}$, and a slit width of $1''$. The resulting dataset consisted of 38 spectroscopic exposures each of 225 s obtained at a spectral resolution of $R \approx 500$. The spectra were reduced using the Gemini IRAF (Image Reduction and Analysis Facility) package. The telluric correction was performed using two standard stars observed together with ULAS J0816+2134 at a similar airmass: HIP 35842 (type A1V, $J = 6.13$ Vega mag) and HIP 50459 (type A0V, $J = 6.54$ Vega mag). The spectra obtained on different dates were reduced and wavelength calibrated independently. The resulting individual 2D spectra were matched in wavelength and stacked. The final 1D spectrum and the error spectrum of ULAS J0816+2134 were obtained from the 2D stack spectrum and its variance. The telluric lines were removed by dividing the 1D spectrum of ULAS J0816+2134 by the 1D spectrum of HIP 35842. The flux of ULAS J0816+2134 was then recovered by multiplying the obtained ratio by the blackbody model of the HIP 50459 spectrum calculated assuming an effective temperature of $T_{\text{eff}} = 9641\text{K}$ reported for this star in the Gaia DR2 catalog (Gaia Collaboration et al. 2018). To improve the signal-to-noise ratio of the detected continuum, the final 1D spectrum was binned to a wavelength resolution of 20\AA corresponding to full width at half-maxima of ~ 480 , ~ 370 , and $\sim 270\text{ km s}^{-1}$ in the J , H , and K bands. The resulting spectrum is presented in Figure 1a. The average signal-to-noise ratios of the spectrum are ~ 3.5 , ~ 3.7 , and ~ 6.9 in the J , H , and K bands, respectively.

3. RESULTS

3.1. Identification of the Emission Lines

The spectrum of ULAS J0816+2134 shows the Ly α $\lambda 1216$ break at $\sim 10420\text{\AA}$ corresponding to an approximate redshift of ~ 7.57 and three emission lines. The emission lines at ~ 13068 and 23698\AA were identified as C IV $\lambda 1549$ and Mg II $\lambda 2799$ both shifted to similar redshifts of ~ 7.44 and 7.46 , respectively (see Figures 1a and 2). The third most prominent emission line detected at $\sim 14982\text{\AA}$ was identified as N III] $\lambda 1750$ redshifted relative to Mg II by $\sim 3500\text{ km s}^{-1}$. As we explain below, this line was identified from the comparison of the spectrum of ULAS J0816+2134 with those of SDSS quasars with strong nitrogen emission lines. In particular, in the catalog of Jiang et al. (2008) of nitrogen-rich

Table 1. Multi-epoch photometry of ULAS J0816+2134.

Survey/ Telescope	UT Obs. Date (yy-mm-dd)	Filter	λ_{eff} (μm)	m_{AB} (AB mag)
UKIRT	2021-02-03	Z	0.88	> 22.78 (5σ)
UKIDSS	2008-11-28	Y	1.03	> 21.10 (5σ)
UKIRT	2021 – 2022	Y	1.03	21.683 ± 0.121
UKIDSS	2007-01-18	J	1.25	> 21.15 (5σ)
UKIDSS	2008-11-28	J	1.25	19.313 ± 0.065
UKIRT	2021-02-03	J	1.25	21.427 ± 0.035
UKIRT	2022-01-27	J	1.25	21.682 ± 0.121
UKIRT	2022-03-13	J	1.25	21.314 ± 0.068
UKIDSS	2008-11-27	H	1.63	21.085 ± 0.123
UKIRT	2021-02-03	H	1.63	21.202 ± 0.087
UKIRT	2022-03-13	H	1.63	21.093 ± 0.126
UKIDSS	2008-11-27	K	2.20	20.573 ± 0.095
UKIRT	2021-02-03	K	2.20	20.603 ± 0.082
UKIRT	2022-03-13	K	2.20	20.611 ± 0.114
WISE	2010 – 2011	$W1$	3.35	20.187 ± 0.173
WISE	2010 – 2011	$W2$	4.60	20.036 ± 0.312
WISE	2010 – 2011	$W3$	11.56	> 17.49 (2σ)
WISE	2010 – 2011	$W4$	22.09	> 15.30 (2σ)

Table 2. Redshifts, spectral slopes ($f_{\lambda} \propto \lambda^{\alpha_{\lambda}}$), and the absolute magnitudes of ULAS J0816+2134 and comparison SDSS quasars.

	z_{MgII}	α_{λ}	M_{1450}
ULAS J0816+2134	7.461 ± 0.007	-0.63 ± 0.44	-25.33 ± 0.07
Comparison SDSS quasars			
SDSS J0916+3908	1.876 ± 0.001	-1.68 ± 0.11	-24.94 ± 0.03
SDSS J1550+4238	2.644 ± 0.008	-0.97 ± 0.10	-24.96 ± 0.03
SDSS J0852+4734	2.428 ± 0.001	-0.71 ± 0.15	-25.06 ± 0.03

quasars discovered by the SDSS survey (the quasars defined as those with the N IV] $\lambda 1486$ and N III] $\lambda 1750$ lines of $\text{EW}_0 > 3\text{\AA}$), we found the quasar SDSS J0852+4734 at $z_{\text{MgII}} = 2.428$ showing the N III], C IV, and Mg II emission lines of similar widths and strengths as those of ULAS J0816+2134. The redshifted and scaled spectrum of SDSS J0852+4734 is overplotted in Figure 1a for comparison.

Additionally, we compared the spectrum of ULAS J0816+2134 with those of quasars SDSS J0916+3908 and SDSS J1550+4238, both of which show the prominent N III] line. The redshifts, spectral slopes, and luminosities of the comparison

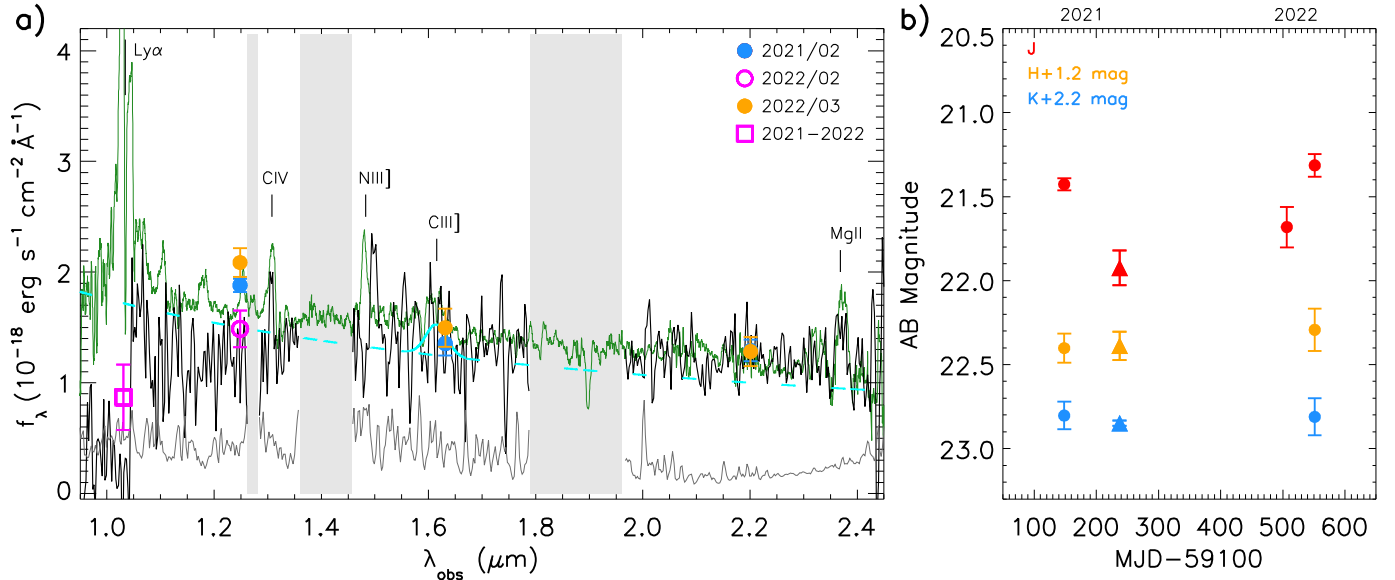


Figure 1. (a) Flux-calibrated Gemini/GNIRS spectrum of ULAS J0816+2134 (black line). The 1σ error spectrum is shown with a gray line. The wavelength intervals affected by strong atmospheric absorption are shaded in light gray. The dashed cyan line represents the $f_\lambda \propto \lambda^{-0.71}$ continuum model. The Gaussian line shown in cyan on the top of the power-law continuum is the Gaussian model of the C III] emission line of ULAS J0816+2134 calculated based on the predicted flux and width of this line. The symbols show the Y -, J -, H -, and K -band fluxes measured at different epochs between 2021 February and 2022 March. Overplotted in green is the scaled and redshift-corrected SDSS spectrum of the low-redshift analog of ULAS J0816+2134, the quasar SDSS J0852+4734 at $z_{\text{Mg II}} \approx 2.428$ from the catalog of nitrogen-rich quasars of Jiang et al. (2008). (b) The J -, H -, and K -band light curves of ULAS J0816+2134 between 2021 February and 2022 March. The magnitudes measured from the UKIRT images are shown with circles. Triangles correspond to the J -, H -, and K -band magnitudes estimated from the flux-calibrated Gemini/GNIRS spectrum.

quasars SDSS J0852+4734, SDSS J0916+3908, and SDSS J1550+4238 are given in Table 2. From the spectra retrieved from the SDSS DR14 public archive (Abolfathi et al. 2018), we found that these quasars show the N III] emission line of $\text{EW}_0 > 10$ (see Figure 3 in Section 3.2) and have absolute magnitudes similar to that of ULAS J0816+2134 (see Table 2). The detailed analysis of the spectra of these quasars revealed that in addition to the narrow central Gaussian-like emission component, the wings of their N III] emission lines show the presence of the underlying broad double-peak emission component. The blueshifted and redshifted emission peaks of the latter component are separated by $\sim 9000 \text{ km s}^{-1}$. Furthermore, the comparison of the SDSS spectra of SDSS J0852+4734 obtained at two different epochs in 2001 and 2012 revealed significant variability of the broad component of its N III] line (see Figure 3). In particular, we find that in 2001 the strength of the blueshifted emission peak of the N III] line of SDSS J0852+4734 was nearly comparable to that of ULAS J0816+2134 (the gray curve in Figure 3), while in 2012 both blueshifted and redshifted emission peaks of SDSS J0852+4734 were relatively weak (the green curve in Figure 3).

The double-peak profiles of the emission lines of quasars similar to that of the N III] line of SDSS J0852+4734, SDSS J0916+3908, and SDSS J1550+4238 are not unusual. Similar line shapes show the profiles of the $\text{H}\alpha$ and $\text{H}\beta$ lines of ~ 3 per cent of broad line quasars (e.g., Eracleous & Halpern 1994; Strateva et al. 2003; Shapovalova et al. 2009; Oknyansky et al. 2021). In the accretion disc wind scenario, the double-peak line profiles are attributed to the emission from the broad line region clouds formed in the outflow from the accretion disk and emitting in the vicinity of the accretion disk plane (e.g., Czerny & Hryniewicz 2011; Elitzur et al. 2014). The double-peak shapes of these lines are usually well reproduced by the emission model of the rotating relativistic disk, which predicts the stronger blueshifted peak and the weaker redshifted peak (e.g., Chen & Halpern 1989; Chen et al. 1989; Eracleous et al. 1995).

Likewise, we attributed the non-Gaussian broad (double-peak) emission component of the N III] line of the quasars SDSS J0852+4734, SDSS J0916+3908, and SDSS J1550+4238 to the emission originating in the close vicinity of the accretion disk. We modelled the N III] line profiles of these quasars both with a single

Gaussian and with the model of the circular relativistic accretion disk using the equations of [Chen & Halpern \(1989\)](#). The resulting modeled profiles are shown in [Figure 3](#) ([Section 3.2](#)). The line profiles predicted by the disk model helped us to explain the large redshift of the N III] line of ULAS J0816+2134 relative its Mg II line. We briefly summarize the parameters of this model. The disk model has five parameters: the inclination angle of the disk i , inner and outer radii of the emitting region r_{inner} and r_{outer} in the units of gravitational radius $r_g = GM_{\text{BH}}/c^2$ (where M_{BH} is the black hole mass and G is the gravitational constant), velocity dispersion σ of the rest-frame Gaussian line profile characterizing local turbulent broadening, and index q of the power-law surface emissivity of the disk $\epsilon(r) \propto r^{-q}$. Following [Eracleous & Halpern \(1994\)](#), the value of the emissivity index was fixed to $q = 3$ expected for local gravitational energy dissipation in the disk (see, e.g., [Chen et al. 1989](#)). The disk model predicts similar inclination angles $i \approx 40^\circ$, velocity dispersions $\sigma \approx 270 \text{ km s}^{-1}$, and $r_{\text{inner}} \approx 1300 r_g$ of the N III] emitting region of SDSS J0852+4734, SDSS J0916+3908, and SDSS J1550+4238, while r_{outer} (which determines the separation between the blueshifted and redshifted peaks) is different for these quasars. We calculated $r_{\text{outer}} \approx 3100, 4600,$ and $2600 r_g$ for the quasars SDSS J0852+4734, SDSS J0916+3908, and SDSS J1550+4238, respectively. For comparison, from the analysis of the double-peak profiles of the H α line of 116 SDSS quasars, [Strateva et al. \(2003\)](#) found disk inclinations in a range of $20^\circ < i < 50^\circ$, inner radii of $r_{\text{inner}} \sim 200 - 800 r_g$, outer radii of $r_{\text{outer}} \gtrsim 2000 r_g$, and turbulent broadening in a range of $780 - 1800 \text{ km s}^{-1}$. Note that the model of the circular rotating relativistic disk does not reproduce the central Gaussian-like emission component of the N III] line of our comparison quasars. A similar central component is also typically present in the double-peak profiles of the H α and H β lines of quasars and is usually fitted separately ([Strateva et al. 2003](#)). This central emission component may originate in a separate region or at higher distances from the disk plane (e.g., [Elitzur et al. 2014](#)).

The N III] emission line of ULAS J0816+2134 overlaps with the red wing of the Gaussian model and also with the redshifted emission peak of the disk model of the N III] line of all three comparison SDSS quasars. As seen in [Figure 3](#), the velocity offset of the N III] line of ULAS J0816+2134 corresponds to the typical velocity offsets of the redshifted emission peaks of the N III] line of the three comparison quasars. We therefore conclude that first, the identification of this line as N III] $\lambda 1750$ was most likely correct. Second, the detected N III] emission

of ULAS J0816+2134 seems to represent only the portion of the line. Namely, it represents the red wing or redshifted disk emission of the line, while the bluer part of the line is not seen, probably due to absorption in the broad line region of the quasar. Thus, as the bluer emission of the line is not detected, the line appears to be significantly redshifted.

The C III] $\lambda 1909$ emission line of ULAS J0816+2134 was not detected. We expect it to be broad ($7500 - 10000 \text{ km s}^{-1}$), similar to the C III] line of the quasars SDSS J0852+4734, SDSS J0916+3908, and SDSS J1550+4238. Assuming that the width and flux of the C III] line of ULAS J0816+2134 is similar to those of the SDSS comparison quasars, the predicted observed flux of this line is $\sim 140 \times 10^{-18} \text{ erg s}^{-1} \text{ cm}^{-2}$ (calculated using the average width and average rest-frame flux of the C III] line of the three comparison quasars). This value is also comparable to the 3σ upper limit on the flux of the C III] line of ULAS J0816+2134 derived in [Section 3.2](#) from the observed spectrum (see [Table 3](#)). The predicted Gaussian profile of the C III] line is shown in [Figure 1a](#). As seen in this figure, the C III] line of ULAS J0816+2134 is likely both too broad and weak to be detected at the signal-to-noise ratio of the current spectrum.

3.2. Properties of the Continuum and Emission Lines

We fitted the continuum of ULAS J0816+2134 with the power-law model representing the UV/optical emission of the accretion disk (e.g., [Malkan & Sargent 1982](#); [Malkan 1983](#)) with the additional contribution from the UV Fe II blended emission lines at $\lambda_{\text{rest}} = 2200 - 3500 \text{ \AA}$:

$$f_\lambda^{\text{cont}} = f_0^{\text{PL}} \lambda^{\alpha_\lambda} + f_0^{\text{Fe}} f_\lambda^{\text{Fe}}, \quad (1)$$

where α_λ is the spectral slope, f_0^{PL} and f_0^{Fe} are the scaling factors of the power-law component and the Fe II emission, and f_λ^{Fe} is the tabulated Fe II UV emission template of [Tsuzuki et al. \(2006\)](#). The spectra of the comparison SDSS quasars were also fitted with this model. We performed several iterations of the fit, each time shifting the Fe II template by the redshift measured from the Mg II line fitted with a Gaussian to the continuum-subtracted spectrum, until the best solution is reached. The Fe II template was broadened to matched the line resolution the Mg II line of ULAS J0816+2134 by convolving with a Gaussian of a full width at half maximum (FWHM) of $\sim 2500 \text{ km s}^{-1}$. The contribution of the Balmer continuum at $\lambda_{\text{rest}} = 2000 - 4000 \text{ \AA}$ representing the emission of partially optically thick clouds (e.g., [Wills et al. 1985](#)) was neglected. From the analysis of the spectra of the comparison SDSS quasars similar to that of [Kurk et al. \(2007\)](#) and

De Rosa et al. (2011), we estimated that the Balmer continuum contributes only $\lesssim 10$ per cent of the power-law component. Additionally, note that accurate modeling of the Balmer continuum of ULAS J0816+2134 and those of the comparison quasars is difficult as their spectra do not cover the Balmer edge at $\lambda_{\text{rest}} = 3646 \text{ \AA}$.

The fit of the UV/optical continuum of ULAS J0816+2134 in the wavelength intervals not affected by emission lines and atmospheric absorption ($\lambda_{\text{rest}} \sim 1550 - 1583, 1949 - 2111, \text{ and } 2323 - 2480 \text{ \AA}$) resulted in a slope of $\alpha_\lambda = -0.63 \pm 0.44$. The spectral slopes of the power-law continua of ULAS J0816+2134 and those of the SDSS quasars are provided in Table 2. We find that within the uncertainty, the continua of ULAS J0816+2134 and quasar SDSS J0852+4734 are remarkably similar across the H and K bands (see Figure 1a). In the J band, the spectrum of ULAS J0816+2134 shows the decrease in the continuum flux at $\lambda_{\text{obs}} \lesssim 1.4 \mu\text{m}$ that may be caused by absorption in the circumnuclear region of the quasar (see Section 4.3). This decrease in flux complicated the continuum fit of ULAS J0816+2134, while that of SDSS J0852+4734 was more robust. Therefore, for the measurement of the properties of the emission lines of ULAS J0816+2134, we adopted a better measured spectral slope of SDSS J0852+4734 of $\alpha_\lambda = -0.71$.

The emission lines of ULAS J0816+2134 were fitted with the Gaussian profiles after subtracting the continuum model from the spectrum. The fitted line profiles of the C IV and Mg II lines are shown in Figure 2. For the Mg II line we obtained two models: the Gaussian model fitted to the power law-subtracted spectrum and the Gaussian model with the contribution from the Fe II UV emission template both of which are shown in Figure 2. The total flux and width of the emission lines were estimated as the Gaussian area and FWHM, respectively. The rest-frame equivalent widths EW_0 of the C IV, N III], and Mg II lines were estimated from the ratio between the observed flux of each line and the underlying continuum corrected for the redshift. The properties of the emission lines are summarized in Table 2, in which the quoted uncertainties are the errors of the fit. For the redshift of the ULAS J0816+2134 we adopted the redshift measured from the Gaussian model of the Mg II line, $z = 7.461 \pm 0.007$.

As discussed in Section 3.1, the profile of the N III] emission line of ULAS J0816+2134 is likely modified by the line-of-sight absorption and the detected line emission may represent only the red wing of the line. Therefore, the flux and equivalent width of the N III] line derived by us from the Gaussian fit should be considered as the lower limits. Even based on the estimated equiv-

Table 3. Total observed fluxes, widths, and rest-frame equivalent widths of the emission lines of ULAS J0816+2134.

Line	$10^{-18} \times F_{\text{line}}$ ($\text{erg s}^{-1} \text{cm}^{-2}$)	FWHM (km s^{-1})	EW_0 (\AA)
C IV $\lambda 1549$	66.4 ± 7.4	1698 ± 275	6.1 ± 0.7
N III] $\lambda 1750$	142.8 ± 4.7	2828 ± 361	12.5 ± 0.4
C III] $\lambda 1909$	$< 137.0^a$	$\sim 8700^a$	$< 16.2^a$
Mg II $\lambda 2799^b$	152.0 ± 14.2	2784 ± 258	17.6 ± 1.8
Mg II $\lambda 2799^c$	118.5 ± 10.9	2434 ± 170	14.3 ± 1.4
Fe II $\lambda 2200 - 3090$	669.6 ± 45.8^d		79.7 ± 6.9

^aThe 3σ upper limits on the flux and equivalent width of the C III] line estimated from the spectrum. The expected line width was estimated as the average line width of the C III] line of the comparison SDSS quasars.

^bBased on the Gaussian model of the Mg II line.

^cBased on the Gaussian model of the Mg II line with the contribution from the Fe II UV emission.

^dThe Fe II UV flux estimated by integrating the flux of the fitted Fe II emission template within an interval of $\lambda_{\text{rest}} = 2200 - 3090 \text{ \AA}$.

alent width of the detected portion of the N III] line ($\text{EW}_0 \sim 12.5 \text{ \AA}$; see Table 2), ULAS J0816+2134 can be classified as a nitrogen-rich quasar (Osmer 1980; Bentz et al. 2004; Jiang et al. 2008).

From the scaled Fe II template, we also estimated the Fe II UV emission flux of ULAS J0816+2134 in the rest-frame interval $2200 - 3090 \text{ \AA}$. This interval was adopted for comparison with the previous measurements of the ion relative abundance in high-redshift quasars (e.g., Kurk et al. 2007; De Rosa et al. 2011). Note, however, that the Fe II UV emission template was scaled using the narrower wavelength interval ($\lambda_{\text{rest}} \sim 2323 - 2858 \text{ \AA}$) than $2200 - 3090 \text{ \AA}$ due to the smaller coverage of the GNIRS spectrum and the influence of atmospheric absorption at $\lambda_{\text{obs}} \sim 18000 - 19500 \text{ \AA}$. The estimated Fe II/Mg II ratio of ULAS J0816+2134 ($\text{Fe II/Mg II} \sim 5.7$) is in relatively good agreement with the mean value $\text{Fe II/Mg II} \sim 3.6 \pm 1.3$ of the nitrogen-rich quasars from the catalog of Jiang et al. (2008) derived using the same Fe II UV emission template.

The M_{1450} absolute magnitude of ULAS J0816+2134 estimated from the flux of the $f_\lambda \propto \lambda^{-0.71}$ continuum at $\lambda_{\text{rest}} = 1450 \text{ \AA}$ is provided in Table 2. The quoted error takes into account the 1σ -uncertainty of the spectrum and uncertainty in the flux calibration of $\sim 0.03 \text{ mag}$.

3.3. Variation of the Near-infrared Flux

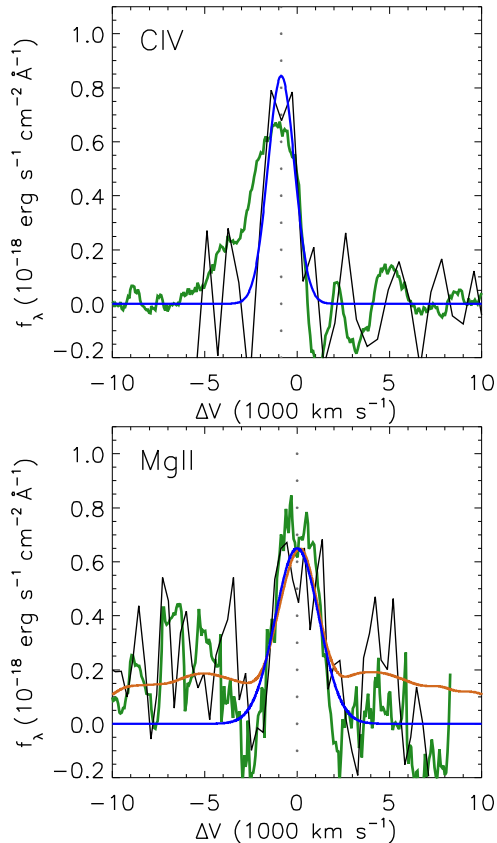


Figure 2. C IV and Mg II line profiles of ULAS J0816+2134 (black lines) after subtracting the underlying power-law continuum model. The Gaussian models of the lines are shown in blue. The Gaussian model of the Mg II line with the contribution from the Fe II UV emission is shown with a brown line. The C IV and Mg II emission lines of the low-redshift quasar SDSS J0852+4734, are overplotted in green for comparison. For this comparison the spectrum of SDSS J0852+4734 was redshift-corrected and normalized to the K -band flux of ULAS J0816+2134. The vertical dotted lines mark the velocity offset relative the Mg II line of ULAS J0816+2134.

The brightness variations of ULAS J0816+2134 are seen in the previous UKIDSS LAS observations of this quasar in 2007 – 2008 and the recent photometric data collected by us between 2021 and 2022. Here, we focused on the analysis of the J , H , and K light curves of the 2021–2022 observing period. These recent data revealed the J -band brightness variations of ULAS J0816+2134 of ~ 0.4 mag on timescales of a few months. During the same 2021 – 2022 epochs, no corresponding brightness variations were detected in the H and K bands (see Figure 1b).

The variations of the UV/optical continua of quasars observed in nearby bands are expected to produce correlated brightness changes of comparable amplitudes.

For comparison, between 2001 and 2012 the flux of the UV/optical continuum of SDSS J0852+4734 changed by approximately the same amount (~ 0.8 mag) at the rest-frame wavelengths corresponding to the J , H , and K bands at the redshift of ULAS J0816+2134. As such correlated variations were not observed in the 2021 – 2022 light curves of ULAS J0816+2134, we concluded that the detected J -band brightness changes were not caused by quasar variability, but most likely have a different origin.

The observational data indicate that the variation of the continuum flux occurs mainly at wavelengths $\lambda_{\text{obs}} \lesssim 1.4 \mu\text{m}$, at which the spectrum of ULAS J0816+2134 shows the signature of absorption. As seen in Figure 1a, at $\lambda_{\text{obs}} \lesssim 1.4 \mu\text{m}$ the UV continuum of ULAS J0816+2134 drops below the flux level predicted by the $f_{\lambda} \propto \lambda^{-0.71}$ continuum model. Since the rest-frame effective wavelength of the J band corresponds to the region of the absorbed continuum ($\lambda_{\text{rest}} \approx 1475 \text{\AA}$), we attributed the observed J -band brightness changes to the variation in the amount of absorption and/or obscuration of the UV continuum emission of the quasar with time.

In Figure 4, we compared the spectral shape of the UV/optical continuum of ULAS J0816+2134 with those of the comparison quasars SDSS J0852+4734 obtained at epochs 2001 and 2012, SDSS J0916+3908, and SDSS J1550+4238. The spectra of these quasars were scaled to the rest-frame K -band flux of ULAS J0816+2134. As seen in this figure, the variation of the rest-frame J -band flux indicates the change of the continuum shape of ULAS J0816+2134 at $\lambda_{\text{rest}} \lesssim 0.17 \mu\text{m}$ from the heavily reddened to the less reddened bluer continuum similar to the continua of the comparison quasars SDSS J0852+4734, SDSS J1550+4238 and SDSS J0916+3908 in the same rest-frame wavelength interval. These variations in the absorbed/obscured continuum flux are usually associated with the line-of-sight variation in the gas column density caused by the motion of the circumnuclear gas clouds of quasars. Thus, the analysis of the multi-epoch X-ray variations of Seyfert galaxies by Risaliti et al. (2002) revealed that the variations in the absorbing column density are quite common among Seyferts. Several studies have also reported the observation of the occultation of the X-ray continuum source by individual clouds in the broad line regions of Seyfert galaxies (e.g., Risaliti et al. 2007, 2009, 2011; Gallo et al. 2021).

Compared to the X-ray emitting region, the UV emitting region of quasars is expected to be less affected by cloud absorption/obscuration due to the larger size. Nevertheless, the photoionization calculations of

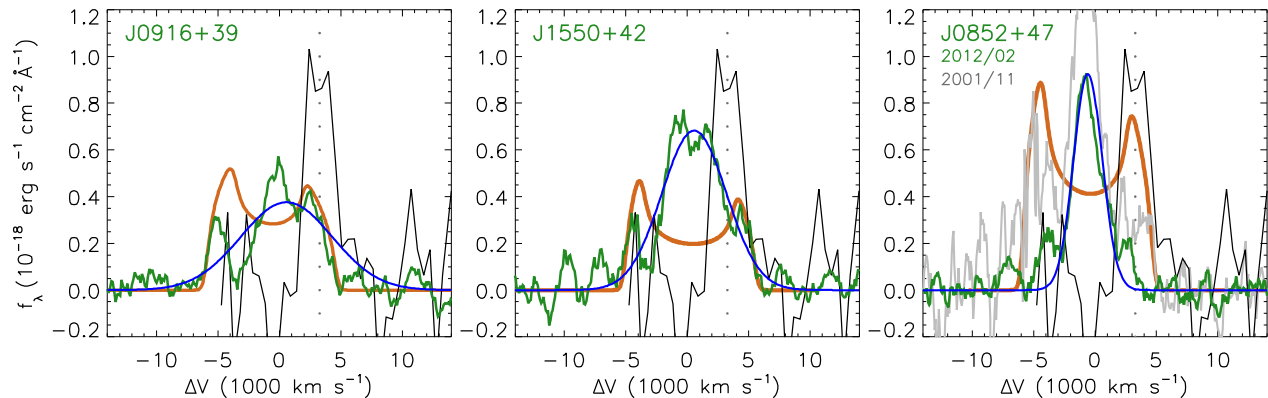


Figure 3. N III] line profile of ULAS J0816+2134 (black lines) in comparison to those of the quasars SDSS J0916+3908 (left panel), SDSS J1550+4238 (middle panel), and SDSS J0852+4734 at epochs 2001 and 2012 (gray and green lines in the right panel). The power-law continuum was subtracted from the line profiles of the quasars. The Gaussian models of the N III] line of SDSS J0916+3908, SDSS J1550+4238, and SDSS J0852+4734 (epoch 2012) are shown with blue lines. The accretion disk models of the N III] line of these quasars are shown with brown lines. The vertical dotted lines mark the velocity offset relative to the Mg II line of ULAS J0816+2134.

Wang et al. (2012) showed that the UV continua of quasars can also be affected by absorption/obscuration by the clouds of the broad line region moving through the line of sight. Moreover, these calculations predict similar absorption features in the obscured continua of quasars as those seen in the rest-frame UV spectrum of ULAS J0816+2134. In Section 4.3, from the amplitude of the observed J -band brightness variations of the rest-frame UV continuum, we constrained the relative variation in the gas column density of ULAS J0816+2134.

4. DISCUSSION

4.1. Black hole mass and Eddington ratio

The method of the SMBH mass measurement of quasars from single-epoch spectra is based on the relation between black hole mass, widths of broad emission lines, and luminosity of the underlying continuum (Vestergaard, M. 2002; Vestergaard & Peterson 2006). This relation was derived from the assumption of the virial motion of gas in the broad line region, $M_{\text{BH}} \sim \text{FWHM}^2 R_{\text{BLR}} G^{-1}$ (where R_{BLR} is the radius of the broad line region), and the empirical relation between continuum luminosity and broad line region radius found from reverberation mapping of low-redshift AGNs, $R_{\text{BLR}} \propto L^\alpha$ (where $\alpha \approx 0.5$; Kaspi et al. 2005; Vestergaard & Peterson 2006). The method is commonly used for the estimation of the mass of the SMBHs of the most distant quasars (e.g., Kurk et al. 2007; De Rosa et al. 2014; Shen et al. 2019), as their spectral properties such as the slope of the UV/optical continuum, the width and relative strength of the broad emission lines, are usually remarkably similar to those

of low-redshift quasars, suggesting a similar physical origin.

To estimate the mass of the SMBH of ULAS J0816+2134, we used the relation of Vestergaard & Osmer (2009) obtained for the Mg II broad emission line:

$$\frac{M_{\text{BH}}}{M_\odot} = 10^{6.86} \left[\frac{\text{FWHM}_{\text{Mg II}}}{1000 \text{ km s}^{-1}} \right]^2 \left[\frac{\lambda L_{\lambda, 3000}}{10^{44} \text{ erg s}^{-1}} \right]^{0.5}, \quad (2)$$

where $\lambda L_{\lambda, 3000}$ is the monochromatic continuum luminosity at $\lambda_{\text{rest}} = 3000 \text{ \AA}$ and $\text{FWHM}_{\text{Mg II}}$ is the width of the Mg II line. The 1σ scatter of this relation is ~ 0.55 dex. As there is evidence that the observed UV continuum of ULAS J0816+2134 is likely reddened by the circumnuclear absorption/obscuration, the UV/optical luminosity of this quasar measured from the observed continuum may be uncertain. We, therefore, estimated the continuum luminosity of ULAS J0816+2134, from the Mg II line using the relation between monochromatic luminosity $\lambda L_{\lambda, 3000}$ and luminosity of the Mg II line of Shen et al. (2011):

$$\log \left(\frac{\lambda L_{\lambda, 3000}}{\text{erg s}^{-1}} \right) = 1.22 + 1.016 \times \log \left(\frac{L_{\text{Mg II}}}{\text{erg s}^{-1}} \right). \quad (3)$$

The 1σ scatter of the relation is ~ 0.16 dex. The bolometric luminosity of ULAS J0816+2134 was then calculated as $L_{\text{bol}} = 5.15 \lambda L_{\lambda, 3000}$ using the bolometric correction factor of Shen et al. (2008). The Eddington ratio was computed as a ratio between the bolometric luminosity L_{bol} and Eddington luminosity $L_{\text{Edd}} = 1.26 \times 10^{38} (M_{\text{BH}}/M_\odot) \text{ erg s}^{-1}$ (Peterson 1997).

The estimated luminosity, black hole mass, and Eddington ratio of ULAS J0816+2134 are summarized in Table 4. This table also provides the SMBH masses and accretion rates of the comparison SDSS quasars from Table 2. The quoted errors were calculated based on the uncertainties of the flux and width of the Mg II line and do not include the uncertainties of relations 2 and 3.

4.2. Nitrogen Abundance and Black Hole Growth History

Both N III] and C III] lines are collisionally excited lines with the comparable critical number densities ($\sim 2 \times 10^{10}$ and $3 \times 10^9 \text{ cm}^{-3}$) and ionization potentials (29.6 and 24.4 eV) (Baldwin, & Netzer 1978; Hamann & Ferland 1999). The ratio of these lines is largely insensitive to the photoionizing conditions such as the ionization parameter and shape of the ionizing continuum and therefore provides a good measurement of the relative abundance of N and C (e.g., Shields 1976).

The N III] line detected in the spectrum of ULAS J0816+2134 suggests a rather high relative abundance of nitrogen in the broad line region of this quasar. The derived 3σ lower limit on the N III]/C III] line ratio is ~ 1 and implies a metallicity of $> 10Z_{\odot}$ (Hamann et al. 2002). Note that the detected N III] emission of ULAS J0816+2134 is likely only the red wing of the total line profile (see the discussion in Section 3.1). Therefore, the measured flux and rest-frame equivalent width of this line should be considered as the lower limits. At the same time, the C III] line is weak. Similar to the bluer portion of the N III] line, C III] may be weakened by absorption. The intrinsic (unaffected by obscuration and absorption) N III]/C III] line ratio of ULAS J0816+2134 is most likely comparable to those of the comparison quasars from Table 2. The N III]/C III] line ratio of these quasars is similarly high as that of ULAS J0816+2134, N III]/C III] = 0.60, 0.98, and 0.60 for SDSS J0916+3908, SDSS J1550+4238, and SDSS J0852+4734, respectively. For comparison, the N III]/C III] line ratio of the composite SDSS quasar spectrum is only $EW_0 \sim 0.44 \text{ \AA}$ (Vanden Berk et al. 2001).

Thus, ULAS J0816+2134 is currently the most distant quasar showing the relatively strong N III] emission line of $EW_0 \gtrsim 12.5 \text{ \AA}$ and one of a few most distant quasars observed at the cosmic age of 0.688 Gyr. As implied by the high relative abundance of nitrogen in the broad line region of ULAS J0816+2134, this quasar is probably seen near the maximum phase of the nitrogen enrichment by the AGB stars, i.e., approximately ~ 0.25 Gyr

after the bulk of star formation (Charlot & Bruzual 1991; Henry et al. 2000; Johnson et al. 2022).

The approximate starburst age of ULAS J0816+2134 implied by the nitrogen abundance provides an independent way to test the history of its black hole. If the initial burst of star formation in the host galaxy of ULAS J0816+2134 occurred at a cosmic age of ~ 0.44 Gyr ($z \sim 10.4$), the active phase of the SMBH growth of this quasar had lasted at most ~ 0.25 Gyr resulting in the final mass of $\sim 5 \times 10^8 M_{\odot}$. Assuming that during this previous ~ 0.25 Gyr, the SMBH of ULAS J0816+2134 was growing at a constant accretion rate of 1, the initial black hole mass of this quasar at the time of the starburst should have been already rather massive, $\sim 3 \times 10^6 M_{\odot}$ (calculated assuming a radiative efficiency of $\epsilon = 0.1$; see Madau et al. 2014). This initial black hole mass favors the scenario of massive initial seeds of the SMBHs of quasars, similar to the other high-redshift quasars found at $z \sim 7.5$ (e.g., Wang et al. 2021).

4.3. Column Density and Size of Obscuring Clouds

The amplitude of the flux variation and the duration of the partial obscuration caused by the motion of the individual absorbing/obscuring clouds of the broad line region through the line of sight of the continuum source provide strong constraints on the column density and linear size of the clouds, e.g., (Risaliti et al. 2007, 2009, 2011; Gallo et al. 2021). As discussed in Section 3.3, the variation of the J -band flux of ULAS J0816+2134 can be attributed to the variation in the absorbing column density caused by the motion of such a cloud. To constrain the column density of the intervening cloud from the observed amplitude of the J -band flux variations, we simulated the model spectra of ULAS J0816+2134 using version 13.03 of the photoionization code CLOUDY (Ferland et al. 1998). For the photoionizing continuum, we employed the standard AGN continuum described in Mathews & Ferland (1987). We then adopted an ionization parameter of $U = 10^{-1.2}$, an average hydrogen number density of the broad line region gas of $n_{\text{H}} = 10^{10} \text{ cm}^{-3}$, and a broad line region radius of $R_{\text{BLR}} = 10^{17} \text{ cm}$. The ionization parameter and gas number density were estimated from the average C III]/C IV line ratio of the comparison quasars SDSS J0852+4734, SDSS J1550+4238, and SDSS J0916+3908, assuming that the photoionization conditions in the broad line region of these quasars are similar to those of ULAS J0816+2134. For the chemical composition of the broad line region gas clouds, we adopted the metallicity equal to $5Z_{\odot}$ (typical for the high-redshift quasars, e.g., Dietrich et al. 2003a,b)

Table 4. Bolometric luminosity, black hole mass, and Eddington ratio of ULAS J0816+2134 and the comparison SDSS quasars.

	ULASJ 0816+2134 ^a	ULASJ 0816+2134 ^b	SDSS J0916+3908	SDSS J1550+4238	SDSS J0852+4734
L_{bol} (10^{46} erg s ⁻¹)	4.35±0.41	3.38±0.31	2.83±0.05	4.36±0.27	3.00±0.10
M_{BH} ($10^8 M_{\odot}$)	5.16±1.02	3.48±0.51	3.59±0.06	4.58±1.25	2.47±0.06
$L_{\text{bol}}/L_{\text{Edd}}$	0.67±0.15	0.77±0.13	0.62±0.02	0.67±0.15	0.96±0.04

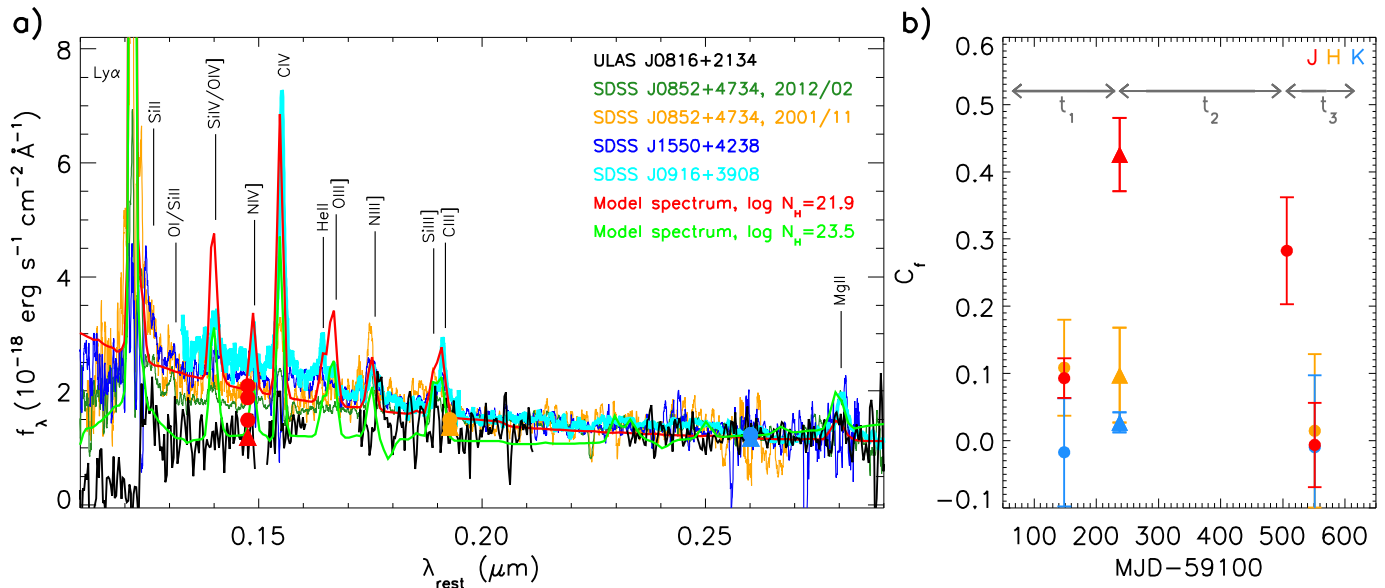
^aBased on the Gaussian model of the Mg II line.^bBased on the Gaussian model of the Mg II line with the contribution from the Fe II UV emission.

Figure 4. (a) Variation of the continuum shape of ULAS J0816+2134 from the spectroscopic observation (black line) and J , H , and K photometry (red, orange, and blue circles, respectively). The J , H , and K fluxes measured from the spectrum of ULAS J0816+2134 are depicted with a red, orange, and blue triangle. The observed variation in the continuum flux of ULAS J0816+2134 is shown in comparison with the spectra of the quasars SDSS J0852+4734 obtained in 2001 and 2012 (orange and green lines), the spectra of SDSS J1550+4238 (blue line), and SDSS J0916+3908 (cyan line) normalized to the K -band continuum flux of ULAS J0816+2134. The spectra predicted by the photoionization models calculated for a column density of the broad line region gas of $N_{\text{H}} = 10^{21.9}$ and $10^{23.5}$ cm⁻² are indicated with a red and light green line. (b) Variation of the covering fraction of the continuum emitting region of ULAS J0816+2134 in the J , H , and K bands during the occultation by an intervening cloud of the broad line region. The circles and triangles correspond to the covering fraction estimated from the J -, H -, and K -band photometry and from the spectrum of ULAS J0816+2134, respectively. The occultation time is divided into time intervals t_1 , t_2 , and t_3 approximately corresponding to the ingress phase, the phase of maximum coverage, and the egress phase of the occultation.

and the metal abundance model of Hamann & Ferland (1993) for an evolving starburst. The hydrogen column density varied in a range of $N_{\text{H}} = 10^{21} - 10^{24}$ cm⁻².

The approximate radius of the broad line region used in the calculations was derived from the typical size of the N III] emitting region of the comparison quasars. It was estimated for an SMBH of $\sim 5 \times 10^8 M_{\odot}$ as $R_{\text{BLR, NIII]}} \sim 2000 r_{\text{g}} \sim 1.5 \times 10^{17}$ cm (see Section 3.1). The relation of Vestergaard & Osmer (2009) for the size

of the Mg II emitting region provides the comparable estimate, $R_{\text{BLR, MgII}} \approx 8.8 \times 10^{17}$ cm.

The calculated model spectra were broadened to match the line width of the comparison SDSS quasars and compared with the spectrum of ULAS J0816+2134 and its J -band flux at different epochs. The model spectra predict the C IV, He II, N III], and C III] emission lines of similar strengths to those of the comparison SDSS quasars. Note however that the model overpredicts the

strengths of the Si IV, O IV], O III], and Si III] emission lines. The latter group of the emission lines may originate at different physical conditions as those assumed by us for the C IV, N III], and C III] emission lines. Here, we only consider the effect of the varying column density on the spectral shape of the UV continuum for the adopted physical conditions.

From the model spectra, we found that the lowest J -band continuum flux corresponds to a column density of $N_{\text{H}} \approx 10^{21.9} \text{ cm}^{-2}$ (see Figure 4a). This model reproduces well the shape of the Gemini/GNIRS spectrum of ULAS J0816+2134, especially at $\lambda_{\text{rest}} \lesssim 0.17 \mu\text{m}$, mostly affected by absorption. Note that the Gemini/GNIRS spectrum was obtained during the lowest J -band continuum flux reduced by line-of-sight absorption/obscuration. The highest J -band continuum flux measured from photometry corresponds to a line-of-sight gas column density of $N_{\text{H}} \approx 10^{23.5} \text{ cm}^{-2}$. Thus, the total variation of the gas column density associated with the observed variation in the J -band flux is $\Delta N_{\text{H}} \approx 10^{23.49} \text{ cm}^{-2}$. The shape of the J -band light curve implies that the actual amplitude of the variation in the column density could have been higher than that provided by the data points. Therefore, we adopted the derived relative column density variation as the lower limit on the column density of the intervening cloud that absorbed/obscured the UV continuum of ULAS J0816+2134. The estimated value is comparable to the column density of the broad line region clouds inferred from the X-ray observations of Seyfert galaxies (e.g., Risaliti et al. 2007, 2009, 2011).

Assuming that the unobscured spectrum of ULAS J0816+2134 is similar to that of the blue simulated spectrum corresponding to $N_{\text{H}} \approx 10^{21.9} \text{ cm}^{-2}$, we estimated the approximate fraction of the obscured J -band flux of the rest-frame UV continuum of ULAS J0816+2134 relative to the flux of the unobscured UV continuum for each of the observational epochs as

$$C_{\text{f}}(t) = \left(1 - \frac{f_J^{\text{J0816}}(t)}{f_J^0} \right), \quad (4)$$

where $f_J^{\text{J0816}}(t)$ and f_J^0 are the J -band flux of ULAS J0816+2134 at epoch t and that of the unobscured continuum model. The variation of the estimated covering fraction of the UV continuum caused by the motion of the intervening cloud through the line of sight of the quasar is shown in Figure 4b. As seen in the figure, the evolution of the covering fraction was relatively smooth. It increased between the first two epochs (February and May 2021) and then decreased between the last two epochs (February and March 2022).

The timescale of the whole variation was ~ 403 d, corresponding to ~ 48 d in the rest-frame of the quasar. The smooth and symmetric shape of the J -band variation in the covering fraction is similar to the covering fraction variation of the X-ray continuum emitting region observed by Risaliti et al. (e.g., 2007); Gallo et al. (e.g., 2021). Following these previous works, we divided the occultation time into time intervals t_1 , t_2 , and t_3 , approximately corresponding to the ingress phase, the phase of maximum coverage, and the egress phase of the occultation (see Figure 2 of Risaliti et al. 2007). The ingress/egress time provides the estimate of the linear cloud size. From the average of the ingress and egress rest-frame time ($t_{1,3} = 0.5 \times (t_1 + t_3) \approx 7.9$) d, we estimated a cloud size of $D_{\text{cl}} = t_{1,3} v_{\text{K}} = 1.7 \times 10^{14} \text{ cm}$, where v_{K} is the Keplerian velocity of the cloud. We assumed $v_{\text{K}} \approx 2500 \text{ km s}^{-1}$, comparable to the width of the Mg II line of ULAS J0816+2134. The size of the UV emitting region corresponding to the rest-frame J -band wavelength ($\lambda_{\text{rest}} \approx 1475 \text{ \AA}$) is then $D_{1475} \approx D_{\text{cl}} \times t_2/t_{1,3} \approx 6.9 \times 10^{14} \text{ cm}$, where $t_2 \approx 32$ d in the quasar rest-frame.

We compared the radius of the continuum source at $\lambda_{\text{rest}} \approx 1475 \text{ \AA}$ derived from the duration of the occultation by the intervening cloud with the half-light radius predicted by the temperature profile of the standard accretion disk of Shakura & Sunyaev (1973) for the same emitting region. Using equation 2 of Blackburne et al. (2011), the estimated half-light radius of the emitting region of ULAS J0816+2134 at $\lambda_{\text{rest}} \approx 1475 \text{ \AA}$ is $R_{1475} \approx 1.6 \times 10^{15} \text{ cm}$ (assuming a radiative efficiency of $\epsilon = 0.1$), which looks comparable within the uncertainties to the size of the continuum emitting region from the occultation light curve. Thus, our assumption about the variation in the covering fraction due to one nearly complete occultation of the UV continuum source of ULAS J0816+2134 detected in the J band is most likely correct despite the relatively poor sampling of the occultation light curve.

5. SUMMARY

We presented the near-infrared spectroscopic and imaging observations, and the data analysis of the newly discovered quasar ULAS J0816+2134 at $z_{\text{MgII}} = 7.461 \pm 0.007$. Based on the detection of the N III] emission line of $\text{EW}_0 \gtrsim 12.5 \text{ \AA}$, ULAS J0816+2134 was classified as a nitrogen-rich quasar. Being the most distant nitrogen-rich quasar and one of the most distant quasars known today, ULAS J0816+2134 provides new independent constraints on the starburst age of the host galaxies and on the growth history of the SMBHs of high-redshift

quasars. We summarize our main results and conclusions as follows:

1. ULAS J0816+2134 is the least luminous of the known $z \sim 7.5$ quasars of an absolute magnitude of $M_{1450} = -25.33 \pm 0.07$. The mass of the SMBH of ULAS J0816+2134 estimated using the Mg II emission line is $M_{\text{BH}} = (5.16 \pm 1.02) \times 10^8 M_{\odot}$ and the Eddington accretion rate is $L_{\text{bol}}/L_{\text{Edd}} = 0.67 \pm 0.15$.

2. The high nitrogen abundance of the broad line region of ULAS J0816+2134 indicates that this quasar is probably seen near the maximum of the nitrogen enrichment of the circumnuclear region by the asymptotic giant branch stars, which implies a starburst age of the host galaxy of ~ 0.25 Gyr. The starburst age provides an independent constraint on the growth timescale and initial mass of the SMBH of ULAS J0816+2134. It implies a sufficiently massive initial black hole mass of $\sim 3 \times 10^6 M_{\odot}$. The appearance of such massive initial black holes in the early Universe is yet to be understood.

3. The flux variation of the observed J -band continuum and the lack of the corresponding variations in the H and K bands, were attributed to the variation in the line-of-sight column density caused by the motion of an intervening broad line region cloud. The amplitude of the observed J -band flux variation implies a cloud column density of $N_{\text{H}} \gtrsim 10^{23.49} \text{ cm}^{-2}$, while the duration of the variation implies a cloud size of $D_{\text{cl}} \approx 1.7 \times 10^{14} \text{ cm}$. The derived column density of the intervening cloud is consistent with the typical column density of mostly neutral, gravitationally bound clouds

of the broad line region of quasars that may fuel the growth of their SMBHs.

ACKNOWLEDGMENTS

This work was supported by the Ministry of Science and Technology of Taiwan, grant Nos MOST 109-2112-M-008-021-MY3 and MOST 110-2112-M-008-021-MY3. Based on data obtained at the international Gemini Observatory, a program of NSF's NOIRLab, via the time exchange program between Gemini and the Subaru Telescope (Program ID: GN-2021A-FT-106). The Subaru Telescope is operated by the National Astronomical Observatory of Japan. The international Gemini Observatory at NOIRLab is managed by the Association of Universities for Research in Astronomy (AURA) under a cooperative agreement with the National Science Foundation on behalf of the Gemini Observatory partnership: the National Science Foundation (United States), National Research Council (Canada), Agencia Nacional de Investigación y Desarrollo (Chile), Ministerio de Ciencia, Tecnología e Innovación (Argentina), Ministério da Ciência, Tecnologia, Inovações e Comunicações (Brazil), and Korea Astronomy and Space Science Institute (Republic of Korea).

Based on observations obtained with UKIRT (Program IDs: U/20B/NCU02, U/21B/NCU01, U/22A/NCU01). UKIRT is owned by the University of Hawaii (UH) and operated by the UH Institute for Astronomy; operations are enabled through the cooperation of the East Asian Observatory.

REFERENCES

- Abolfathi, B., Aguado, D. S., Aguilar, G., et al. 2018, *ApJS*, 235, 42
- Araki, N., Nagao, T., Matsuoka, K., et al. 2012, *A&A*, 543, A143
- Baldwin, J. A., & Netzer, H. 1978, *ApJ*, 226, 1
- Bañados, E., Venemans, B. P., Decarli, R., et al. 2016, *ApJS*, 227, 11
- Bañados, E., Venemans, B. P., Mazzucchelli, C., et al. 2018, *Nature*, 553, 473-476
- Batra, N. D., & Baldwin, J. A. 2014, *MNRAS*, 439, 771-787
- Bentz, M. C. Hall, P. B., & Osmer, P. S. 2004, *AJ*, 128, 561
- Blackburne, J. A., Pooley, D., Rappaport, S., & Schechter, P. L. 2011, *ApJ*, 729, 34
- Chambers, K. C., Magnier, E. A., Metcalfe, N., et al. 2016, eprint arXiv:1612.05560
- Charlot, S., & Bruzual, A. G. 1991, *ApJ*, 367, 126
- Chen, K., Halpern, J. P., & Filippenko, A. V. 1989, *ApJ*, 339, 742
- Chen, K., & Halpern, J. P. 1989, *ApJ*, 344, 115
- Cutri, R. M., Wright, E. L., Conrow, T., et al. 2014, *VizieR Online Data Catalog*, II/328
- Czerny, B., & Hryniewicz, K. 2011, *A&A*, 525, L8
- Davies, R. I., Müller Sánchez, F., Genzel, R., et al. 2007, *ApJ*, 671, 1388
- De Rosa, G., Decarli, R., Walter, F., et al. 2011, *ApJ*, 739, 56
- De Rosa, G., Venemans, B. P., Decarli, R., et al. 2014, *ApJ*, 790, 145
- Dietrich, M., Appenzeller, I., Hamann, F., et al. 2003a, *A&A*, 398, 891
- Dietrich, M., Hamann, F., Shields, J. C., et al. 2003b, *ApJ*, 589, 722
- Edmunds, M. G., & Pagel, B. E. J. 1978, *MNRAS*, 185, 77-80
- Elias, J. H., Joyce, R. R., Liang, M., et al. 2006, *Proc. SPIE*, 6269, 138

- Elitzur, M., Ho, L. C., & Trump, J. R. 2014, *MNRAS*, 438, 3340-3351
- Eracleous, M., & Halpern, J. P. 1994, *ApJS*, 90, 1
- Eracleous, M., Livio, M., Halpern, J. P., & Storchi-Bergmann, T. 1995, *ApJ*, 438, 610
- Ferland, G. J., Korista, K. T., Verner, D. A., et al. 1998, *PASP*, 110, 761
- Gallo, L. C., Gonzalez, A. G., & Miller, J. M. 2021, *ApJL*, 908, L33
- Gaia Collaboration, Brown, A. G. A., Vallenari, A., et al. 2018, *A&A*, 616, A1
- Gaskell, C. M. 2009, *NewAR*, 53, 140
- Hamann, F., & Ferland, G. 1992, *ApJL*, 391, L53
- Hamann, F., & Ferland, G. 1993, *ApJ*, 418, 11
- Hamann, F., & Ferland, G. 1999, *ARA&A*, 37, 487
- Hamann, F., Korista, K. T., Ferland, G. J., Warner, C. & Baldwin, J. 2002, *ApJ*, 564, 592
- Henry, R. B. C., Edmunds, M. G., & Köppen, J. 2000, *ApJ*, 541, 660
- Hewett, P. C., Warren, S. J., Leggett, S. K., & Hodgkin, S. T. 2006, *MNRAS*, 367, 454
- Inayoshi, K., Visbal, E., & Haiman, Z. 2020, *ARA&A*, 58, 27
- Jiang, L., Fan, X., Vestergaard, M., et al. 2007, *AJ*, 134, 1150
- Jiang, L., Fan, X., & Vestergaard, M. 2008, *ApJ*, 679, 962
- Jiang, L., McGreer, I. D., Fan, X., et al. 2016, *ApJ*, 833, 222
- Johnson, J. W., Weinberg, D. H., Vincenzo, F., Bird, J. C. & Griffith, E. J. 2022, arXiv:2202.04666, *MNRAS*, submitted
- Juarez, Y., Maiolino, R., Mujica, R., et al. 2009, *A&A*, 494, L25
- Kaspi, S., Maoz, D., Netzer, H., et al. 2005, *ApJ*, 629, 61
- Koptelova, E., Hwang, C.-Y., Malkan, M. A., Yu, P.-C. 2019, *ApJ*, 882, 144
- Koptelova, E., & Hwang, C.-Y. 2022, *ApJL*, 929, L7
- Kurk, J. D., Walter, F., Fan, X., et al. 2007, *ApJ*, 669, 32
- Kurk, J. D., Walter, F., Fan, X., et al. 2009, *ApJ*, 702, 833
- Lawrence, A., Warren, S. J., Almaini, O., et al. 2007, *MNRAS*, 379, 1599
- Madau, P., Haardt, F., & Dotti, M. 2014, *ApJ*, 784, L38
- Maiolino, R., Juarez, Y., Mujica, R., Nagar, N. M., & Oliva, E. 2003, *ApJL*, 596, L155-L158
- Malkan, M. A. & Sargent, W. L. W. 1982, *ApJ*, 254, 22-37
- Malkan, M. A. 1983, *ApJ*, 268, 582-590
- Marziani, P., del Olmo, A., Perea, J., D’Onofrio, M., & Panda, S. 2020, *Atoms*, 8, 94
- Mathews, William G., & Ferland, G. J. 1987, *ApJ*, 323, 456
- Matsuoka, K., Nagao, T., Maiolino, R., Marconi, A., & Taniguchi, Y. 2009, *A&A*, 503, 721-730
- Matsuoka, K., Nagao, T., Marconi, A., Maiolino, R., & Taniguchi, Y. 2011, *A&A*, 527, A100
- Matsuoka, K., Nagao, T., Maiolino, R., et al. 2017, *A&A*, 608, A90
- Matsuoka, Y., Iwasawa, K., Onoue, M., et al. 2019, *ApJ*, 883, 2
- Matsuoka, Y., Iwasawa, K., Onoue, M., et al. 2022, *ApJS*, 259, 18
- Mazzucchelli, C., Bañados, E., Venemans, B. P., et al. 2017, *ApJ*, 849, 91
- Mortlock, D. J., Warren, S. J., Venemans, B. P., et al. 2011, *Nature*, 474, 616-619
- Nagao, T., Marconi, A., & Maiolino, R. 2006, *A&A*, 447, 157
- Nagao, T., Maiolino, R., & Marconi, A. 2006, *A&A*, 447, 863-876
- Netzer, H. 2008, *NewAR*, 52, 257
- Oknyansky, V. L., Brotherton, M. S., Tsygankov, S. S., et al. 2021, *MNRAS*, 505, 1029
- Onoue, M., Bañados, E., Mazzucchelli, C., et al. 2020, *ApJ*, 898, 105
- Osmer, P. S. 1980, *ApJ*, 237, 666
- Padovani, P. & Matteucci, F. 1993, *ApJ*, 416, 26
- Peterson, B. M. 1997, *An Introduction to Active Galactic Nuclei* (Cambridge: Cambridge Univ. Press)
- Reed, S. L., Banerji, M., Becker, G. D., et al. 2019, *MNRAS*, 487, 1874
- Risaliti, G., Elvis, M., & Nicastro, F. 2002, *ApJ*, 571, 234-246
- Risaliti, G., Elvis, M., Fabbiano, G., et al. 2007, *ApJL*, 659, L111
- Risaliti, G., Miniutti, G., Elvis, M., et al. 2009, *ApJ*, 696, 160
- Risaliti, G., Nardini, E., Salvati, M., et al. 2011, *MNRAS*, 410, 1027
- Schindler, J.-T., Farina, E. P., Bañados, E., et al. 2020, *ApJ*, 905, 51
- Shakura, N. I., & Sunyaev, R. A. 1973, *A&A*, 24, 337
- Shapovalova, A. I., Popović, L. Č., Bochkarev, N. G., et al. 2009, *NewAR*, 53, 191
- Shen, Y., Greene, J. E., Strauss, M. A., Richards, G. T., & Schneider, D. P. 2008, *ApJ*, 680, 169
- Shen, Y., Richards, G. T., Strauss, M. A., et al. 2011, *ApJS*, 194, 45
- Shen, Y., Wu, J., Jiang, L., et al. 2019, *ApJ*, 873, 35
- Shields, G. A. 1976, *ApJ*, 204, 330
- Strateva, I. V., Strauss, M. A., Hao, L., et al. 2003, *AJ*, 126, 1720
- Tsuzuki, Y., Kawara, K., Yoshii, Y., et al. 2006, *ApJ*, 650, 57

- Valiante, R., Schneider, R., Bianchi, S., & Andersen, A. C. 2009, *MNRAS*, 397, 1661-1671
- Vanden Berk, D. E., Richards, G. T., Bauer, A., et al. 2001, *AJ*, 122, 549
- Venemans, B. P., Findlay, J. R., Sutherland, W. J., et al. 2013, *ApJ*, 779, 24
- Venemans, B. P., Verdoes Kleijn, G. A., Mwebaze, J., et al. 2015, *MNRAS*, 453, 2259-2266
- Vestergaard, M. 2002, *ApJ*, 571, 733
- Vestergaard, M., & Peterson, B. M. 2006, *ApJ*, 641, 689
- Vestergaard, M., & Osmer, P. S. 2009, *ApJ*, 699, 800
- Vincenzo, F., & Kobayashi, C. 2018, *A&A*, 610, L16
- Vincenzo, F., & Kobayashi, C. 2018, *MNRAS*, 478, 155-166
- Wang, Y., Ferland, G. J., Hu, C., Wang, J.-M., & Du, P. 2012, *MNRAS*, 424, 2255
- Wang, F., Yang, J., Fan, X., et al. 2018, *ApJL*, 869, L9
- Wang, F., Yang, J., Fan, X., et al. 2019, *ApJ*, 884, 30
- Wang, F., Yang, J., Fan, X., et al. 2021, *ApJL*, 907, L1
- Wills, B. J., Netzer, H., & Wills, D. 1985, *ApJ*, 288, 94-116
- Willott, C. J., Delorme, P., Reylé, C., et al. 2010, *AJ*, 139, 906
- Willott, C. J., Albert, L., Arzoumanian, D., et al. 2010, *AJ*, 140, 546
- Wright, E. L., Eisenhardt, P. R. M., Mainzer, A. K., et al. 2010, *AJ*, 140, 1868
- Yang, J., Wang, F., Fan, X., et al. 2019, *AJ*, 157, 236
- Yang, J., Wang, F., Fan, X., et al. 2020, *ApJL*, 897, L14